Journal of Materials Chemistry A

Accepted Manuscript

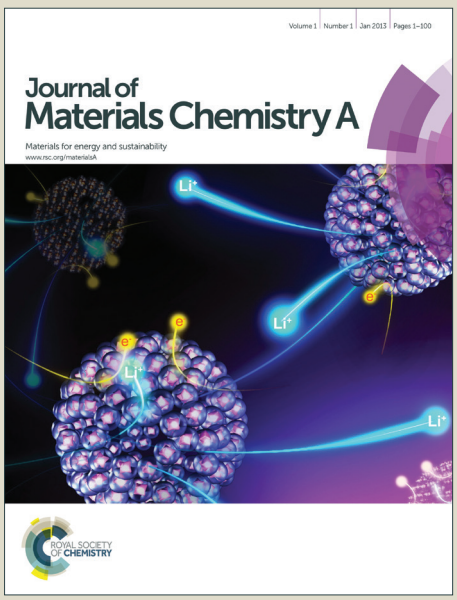

ROYAL SOCIETY OF CHEMISTRY

www.rsc.org/materialsA

Cite this: DOI: 10.1039/c0xx00000x

www.rsc.org/xxxxxx

ARTICLE TYPE

One-step synthesis of SnO_x nanocrystalline aggregates encapsulated by amorphous TiO_2 as anode in Li-ion battery

Xiaoyu Hou,[a] Yanjie Hu,*[a] Hao Jiang,[a] Yunfeng Li,[b] Wenge Li[a] and Chunzhong Li*[a]

Received (in XXX, XXX) Xth XXXXXXXXX 20XX, Accepted Xth XXXXXXXXX 20XX

DOI: 10.1039/b000000x

SnO_x nanocrystalline aggregates (NAs) encapsulated by amorphous TiO_2 layer have been successfully designed by a one-step flame spray pyrolysis (FSP). The synthesized SnO_x NAs@TiO_2 with different degrees of aggregations are composed of SnO_x nanocrystallines ranging from 5 nm to 10 nm and TiO_2 layer with 1-5nm thickness. The encapsulated TiO_2 layer is in situ introduced by incorporating $TiCl_4$ into the downstream of FSP reactor where TiO_2 nucleate and grow in the surface of SnO_x NAs. The hydrolysis temperature of $TiCl_4$ in flame has been controlled to synthesize amorphous TiO_2 with intrinsic electrochemical features. As anode in LIBs (Li-ion batteries), the SnO_x NAs@TiO_2 electrode show superior cycle life and rate performance (350 mA h g^{-1} after 300 cycles, 332 mA h g^{-1} at 1 A g^{-1}) compared to pure SnO_x or TiO_2 electrode. The remarkably enhanced Li^+ storage performance is mainly contributed to nanoscale of nanocrystalline aggregates，core-shell structure of SnO_x@TiO_2 and the amorphous state of TiO_2.

Introduction

Lithium-ion batteries (LIBs) are considered as one of widely consumed and important energy storage device owing to its advantages of high voltage, high energy density, no memory effect, long cycle life and environmental friendly.[1-3] In the past decades, great efforts have been made to realize the increasing market demand on high performance LIBs. Modern Li-ion batteries hold more than twice as much energy by weight as the first commercial versions sold by Sony in 1991 and the pursuit of higher energy density with longer cycle life has never been stopped.[4-6] Among available anode materials, SnO_x-based materials (i.e., Sn, SnO, SnO_2) are deemed as one of promising alternative material because of high theory energy density (780 $mAgh^{-1}$ for SnO_2, 875 $mAgh^{-1}$ for SnO, 990 $mAgh^{-1}$ for Sn), which are much larger than that of graphite materials (372 $mAgh^{-1}$).[7,8] However, the pulverization and deterioration of active materials easily result in the capacity fading and poor cycle life owing to huge volume expansion/shrink in the $LiSn_x$ alloy/dealloy reaction, further limiting the application of SnO_x-based materials in LIBs.[9-12]

Several strategies have been employed to overcome this issue, such as particle size control, coupling another with component (eg, carbon) and the design of unique structure.[13] Generally, reducing the primary particle size to nanoscale has been recognized as a valuable approach toward alleviating the deleterious effects of volume expansion, especially for SnO_x-based materials.[14-16] On the other hand, incorporating another material to form core-shell structure which could suffer $LiSn_x$ volume expansion is necessary. For instance, TiO_2 is one excellent anode material with advantages of cycling stability, low cost and environmental friendly.[17,18] It have been demonstrated that TiO_2 could achieve energy storage by insertion Li^+ ions with nearly zero volume change, making it suitable as backbone or protective layer for SnO_x to restrain the pulverization. Recently, a variety of SnO_x@TiO_2 core-shell composites have been successfully synthesized, realizing enhanced electrochemistry performance compared to pure SnO_x-based electrode.[19-23] For instance, Jeun[22] reported that SnO_2@TiO_2 double-shell nanotubes fabricated by atomic layer deposition exhibited excellent high rate cyclability even the current density reach as high as 1.5 Ag^{-1}. Ji[23] and his coworkers demonstrated as-prepared SnO_2@TiO_2 nanostructured composite was regarded as a high-power-energy anode material, which presented 735 mA h g^{-1} at 1 A g^{-1} in the first cycle and 505 mA h g^{-1} at the end of 30 cycles. However, as-prepared TiO_2 were rutile or anatase in crystalline state. The insertion of lithium into bulk rutile TiO_2 is anisotropic, preventing the lithium ions from reaching favorable sites.[24] For anatase TiO_2, two phases, a lithium-poor phase ($Li_{0.01}TiO_2$) and a lithium-rich phase ($Li_{0.6}TiO_2$), are easily formed and lithium ions diffusion can occur at the boundary, which limits the rate of the insertion of lithium ions.[25,26] Recently, amorphous TiO_2-derived Li_xTiO_2 has a higher rate capacity than anatase TiO_2 with similar morphology and structure, implying that lithium ions diffuses more rapidly in amorphous Li_xTiO_2.[27] However, amorphous TiO_2 could easily convert into anatase or rutile crystal during the subsequent calcination, which makes the encapsulation of amorphous layer be more difficult to control.

Flame spray pyrolysis (FSP) has been demonstrated to be an effective vapor-phase route for the design of nanomaterials.[28-31] Compared to liquid-phase route, flame synthesis has advantages of being continues, rapid, scalable and without post-treatment. Specifically, in a modified FSP equipment, a another different

component can be brought in the downstream of flame through a quenching ring device to design unique core-shell heterogeneous composite, such as Fe_2O_3@SnO_2,[32] TiO_2@SnO_2,[33] SnO_2@TiO_2,[34] In particular, our previous work has already demonstrated that amorphous TiO_2 layer could be realized in SnO_2 nanorod@TiO_2 nanocomposite by controlling the hydrolysis reaction of $TiCl_4$ in flame. Although the reaction temperature is higher than 450 ^oC, the extremely short residence time leads to the encapsulation of amorphous TiO_2 on the surface of SnO_2 nanorod in a rapid process.

In this work, SnO_x nanoaggregates consist of SnO_x nanocrystals under 10nm size were encapsulated by amorphous TiO_2 to prepare SnO_x NAs@TiO_2 by FSP. During the flame process, tin precursor is firstly decomposed into SnO_x aggregates, following with in situ encapsulating of TiO_2 on the SnO_x aggregates by incorporating titanium tetrachloride through a quenching ring. The hydrolysis temperature of titanium tetrachloride has been controlled under 500 ^oC by adusting the height of quenching ring above the flame to obtain amorphous TiO_2. The as-prepared SnO_x NAs@TiO_2 has three advantages of employing as electrode materials in LIBs: ultrasmall size of SnO_x nanocrystals, confinement of SnO_x inside TiO_2 layer, and the amorphous TiO_2 with intrinsic structural features. Besides, the preparation method of SnO_x NAs@TiO_2 is a one-step flame process with simple, continuous and rapid merits, revealing the potential of the large-scale production.

Experimental

Synthesis of SnO_x NAs @TiO_2

In a typical experiment, 0.2 mol/L stannous octoate ($C_{16}H_{30}O_4Sn$, Sinopharm chemical reagent Co., Ltd., AR) dissolved in ethanol (50 mL) were employed as precursor solution. The precursor solution was fed at 5 mL min^{-1} through a spray nozzle and dispersed by external 5 L min^{-1} O_2, forming a fine spray with a diffuse pressure of 0.06 MPa. Then the spray was ignited and supported by H_2/O_2 flame. The flame combustion atmospheres were controlled by adjusting the flow of 1.14 m^3 h^{-1} H_2 and 1.0 m^3 h^{-1} air. The FSP reactor was enclosed in a stainless steel pipe (D =5 cm, L = 100 cm), and a stainless steel metal torus pipe ring with 16 radial equispaced openings (1mmi.d. each, angled 20 upwards from the centerline was fixed 40 cm above the nozzle (Schematic diagram of FSP process was shown in the ESI, Fig. S1).

Firstly, the SnO_x NAs was synthesized by the flame pyrolysis of a 0.2 M precursor solution of $C_{16}H_{30}O_4Sn$ in ethanol. The fresh SnO_x was then in situ encapsulated by TiO_2 nanocrystallines with assistance of anhydrous N_2 carrying titanium tetrachloride ($TiCl_4$, Sinopharm chemical reagent Co., Ltd., AR) vapor through the 16 openings in the pipe ring. The $TiCl_4$ vapor source was supplied by 1 L min^{-1} N_2 through a bubble bottle immersed in water at 30 ^oC. An additional 10 L min^{-1} N_2 was pre-mixed with carry gas N_2 in the pipe ring for better mixing of SnO_x and $TiCl_4$. Owing to high temperature in the reactor, the $TiCl_4$ vapor rapidly hydrolyzed into TiO_2 nanocrystalline on the surface of SnO_x NAs. Finally, the fresh products were collected by a glass filter (ADVTECH/GA55, Toyo Roshi Kaisha Ltd. Japan) in the downstream of FSP equipment with the aid of a vacuum pump.

Materials Characterizations

The samples were characterized by Field emission scanning electron microscopy (FE-SEM: HITACHI S-4800) with energy dispersive X-ray spectroscopy (EDS), Transmission electron microscope (TEM: JEOL JEM-1400), High resolution Transmission electron microscope (HRTEM: JEOL JEM-2100), X-ray diffraction (XRD: D/max 2550V) and Thermogravimetric Analysis (TG: NETZSCH STA409PC). Nitrogen adsorption–desorption (ASAP 2010N) was determined by the Brunauer–Emmett–Teller (BET) method. X-ray photoelectron spectroscopy (XPS) experiments were carried out by Thermo Fisher (ESCALAB 25).

Electrochemical Measurements

The working electrode was composed of active materials (SnO_x NAs@TiO_2, SnO_x NAs and TiO_2 NAs), conductive material (acetylene black, AB) and binder (polyvinyldifluoride, PVDF) with a weight ratio of 80:10:10. The three components were stirred into slurry with assistance of N-methyl-2-pyrrolidone (NMP) and uniformly pasted on Cu foils (19 μm) with a controllable membrane thickness of 50 μm. Thin Li foils (φ16×1.2 mm) and polypropylene membrane (Celgard 2400) were employed as the counter electrode and separator, respectively. The electrolyte was 1 M $LiPF_6$ dissolved in ethylene carbonate/diethyl carbonate (EC-DEC, 1:1 w/w). The half-cells (CR2016 coin type) were employed and assembled in a high-purity argon filled glove box (Mikrouna Advanced Series) where moisture and oxygen levels were under 1 ppm. Cyclic voltammograms (CV) and electrochemical impedance spectroscopy (EIS) of the working electrode had been characterized by electrochemical workstation (Autolab PGSTAT302N). Galvanostatic cycle perfomance of coin cells were tested using on a LAND-CT2001C test system at several different current densities (from 100 mA h g^{-1} to 1000 mA h g^{-1}) in the voltage range from 0.01 V to 2.0 V.

Results and discussion

The structure and morphology of as-prepared SnO_x NAs@TiO_2 were confirmed by TEM as shown in Fig. 1. It was obviously seen in the low magnification TEM images that the as-prepared nanocrystallines assembled into aggregations with different volumes. This could be mainly ascribed to extremely rapid process of FSP (less than 1 second residence time from primary particle to aggregates). The inferior voids could also be found in the aggregates, which may be beneficial to Li^+ ions diffusions. Most of the nanoparticles in the SnO_x NAs@TiO_2 are smaller than 10 nm, which is further confirmed by macroscopic TEM images in Fig. 1b. Moreover, the larger macroscopic TEM was supported and the particle size distribution is ranging from 100 nm to 150 nm, demonstrating the intrinsic nature of aggregates (Fig. S2). For further demonstrating of crystal and structural nature of SnO_x NAs@TiO_2, the high magnification TEM and SAED pattern were shown in Fig.1b, c. The amorphous TiO_2 layer with 1-5 nm thickness could be reasonably distinguished from the high crystallinity SnO_x nanocrystallines inside of aggregates. The

SAED pattern showed concentric circles shape, indicating the SnO_x NAs@TiO_2 was polycrystalline. The crystal lattice distances are measured to be 0.33 nm and 0.30 nm, representing the (101) plane of SnO and (110) plane of SnO_2, respectively. The SnO_x NAs is consist of 80 wt% SnO_2 and 20 wt% SnO calculated by TGA data (Fig. S3). For better understanding of core-shell structure of SnO_x NAs@TiO_2, elemental mapping with element Ti, Sn and O was demonstrated to verify the elements distribution. As shown in the Fig. 1d, the Ti element distribution was almost overlapped with the Sn distribution while the area of Ti was a little larger than that of Sn. Incorporating elemental mapping with HR-TEM, we may safely draw the conclusion that the SnO_x NAs was homogeneously encapsulated by TiO_2.

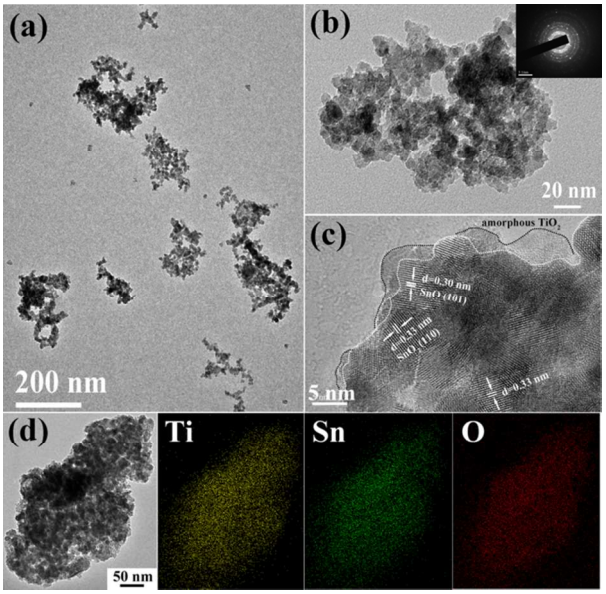

Fig. 1 TEM images (a,b) and HR-TEM image (c) of SnO_x NAs@TiO_2; TEM along with elemental mapping of Ti, Sn, O, respectively (d).

The macroscopic structure and morphology of prepared SnO_x NAs@TiO_2 was characterized by FE-SEM. Due to the extremely high temperature and short particle residence time in flame, most common flame-synthesized nanomaterials are spherically shaped primary particles with different degrees of agglomeration.[30,31] As shown in Fig. 2a, a lot of SnO_x nanoparticles adhered together physically and became into larger agglomerations. The degrees of aggregate or agglomeration varies differently most influenced by the competition relations between coagulation and coalescence in flame. So far, to accurately control the aggregation of nanoparticles in flame was still an on-going subject for the design of nanomaterials. The specific surface area of SnO_x NAs@TiO_2 was 54.7 $m^2 g^{-1}$ with pore diameter of 10-100 nm (Fig. S4). For more understanding of distribution of element on SnO_x NAs@TiO_2, Elemental mapping of Ti, Sn, O were exhibited in Fig. 2c, 2d and 2e. It was obviously noted that Ti, Sn, O elements was uniformly distributed on the NAs, indicating that TiO_2 was finely encapsulated on the surface of SnO_x NAs.

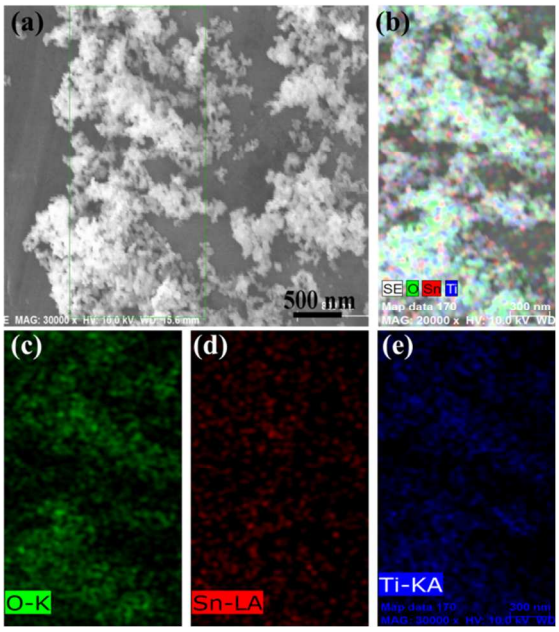

Fig.2 SEM images of SnO_X NAs@TiO_2 (a,b); Elemental mapping of O, Sn, Ti, respectively (c-e).

The XRD pattern of SnO_x NAs@TiO_2 had been employed to identify the crystallographic phases. As shown in Fig.3, the distinctive diffraction peaks of pristine sample can be matched to SnO (JCPDS No.04-0551) and SnO_2 (JCPDS No.41-1445) while no rutile or anatase TiO_2 reflection profiles could be observed. This was mainly attributed to a rapid process of encapsulation of TiO_2 with relatively low reaction temperature (<500 ^oC). When the pristine sample had been post-thermal-treated at 800 ^oC for 2h in Ar, the strong diffraction peaks of rutile TiO_2 could be easily found, indicating that the amorphous TiO_2 existed on pristine SnO_x NAs@TiO_2. Based on Scherrer's equation, the average size of SnO_x NAs@TiO_2 was 11.6 nm，which was larger than the Statistical results from TEM.

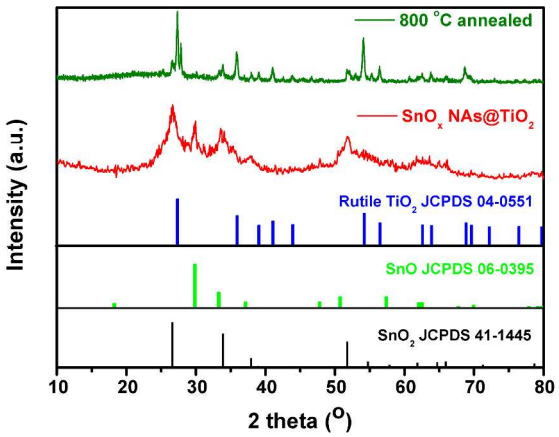

Fig. 3 XRD pattern of as-prepared SnO_x NAs@TiO_2.

XPS analysis was conducted to obtain more information on the chemical states of as-prepared SnO_x NAs@TiO_2. Fig. 4 presented signals of Sn, Ti, O elements on XPS spectra. The Sn 3d5/2 peak consisted of two different chemically shifted components (Fig. 4a). The components at 487.5 eV and 486.7 eV were attributed to Sn^{4+} and Sn^{2+} of Sn element, respectively, further confirming the

presence of SnO_2 and SnO. The weight ratio of Sn^{4+}/Sn^{2+} is 25%/75% calculated by XPS, which was quite different from the TGA data (80 wt%/20 %wt, Fig. S3). This might be mainly ascribed to the surface detection of XPS on the sample. The peaks located at 458.5 eV and 463.9 eV in the Ti2p scan (Fig. 4b) should be attributed to the levels of $Ti2p_{3/2}$ and $Ti2p_{1/2}$ spin-orbital splitting photoelectrons in the Ti^{4+} chemical state, respectively. The O 1s could be deconvoluted into three peaks (Fig. 4d): one at 531.7 eV possibly originated from C-O binding, one at 530.6 eV may be attributable to bonding of Sn-O, and the other one at 530.1 eV could result from Ti-O bonding of TiO_2.

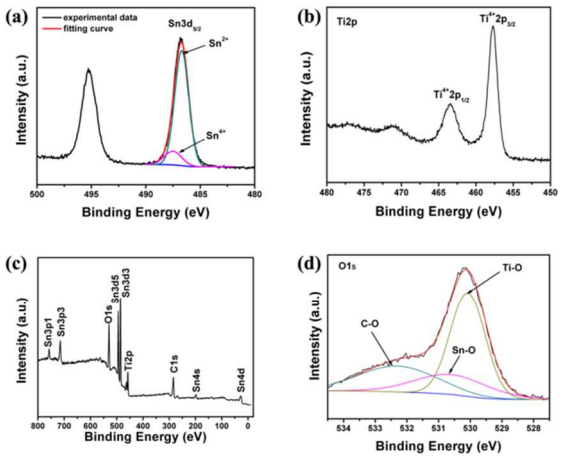

Fig. 4 XPS Sn 3d narrow scan spectra for SnO_x NAs@TiO_2 (a); XPS Ti 2p spectra for SnO_x NAs@TiO_2 (b); XPS general spectra (c); XPS O1s spectra (d).

The as-prepared SnO_x NAs@TiO_2 with ultrasmall size (every nanocrsytal less than 10nm), core-shell structure with TiO_2 protection layer and amorphous state of TiO_2, was supported to perform excellent electrochemical properties in LIBs. The CV profile of SnO_x NAs@TiO_2 electrode was carried out in the voltage range of 0.01-2.5 V (versus Li/Li^+) at a scanning rate of 0.2 mV s^{-1} (Fig. 5a). In the first cathodic sweep, the peaks between 0.25 V and 0.62 V were attributed to multistep lithiation reaction of Sn with Li to form Li_xSn alloys while strong peaks at the anode scanning between 0.5 V and 0.8 V can be assigned to delithiation of the Li_xSn alloy.[35,36] The oxidation peaks between 0.5 V and 0.8 V were almost overlapped in the first three cycles and demonstrated a reversible Li^+ deintercalation from the Li_xSn alloy. Moreover, the initial scan on the negative-current side showed a broad reduction peak from 0.75 V to 1.25 V, which was different from the following two scans. The irreversible peaks were mainly contributed to the formation of solid electrolyte interphase (SEI) films and Li_2O adhering to on the surface of SnO_x NAs@TiO_2.[37] A broad peak between 1.0 V and 2.0 V could be assigned to the insert of Li^+ into amorphous TiO_2, forming Li_xTiO_2.[36] This observation further confirmed a different mechanism of Li^+ insertion from anatase or rutile TiO_2, which usually have two independent peaks at 1.7 V and 2.1 V, respectively.

The voltage vs. capacity profiles of SnO_x NAs@TiO_2 anode at a current density of 200 mA h g^{-1} between 0.01 V and 2.0 V was characterized in Fig. 5b. The voltage drop steeply to 1.5 V in the first discharge scan and a voltage plateau around 1.45 V were appeared and disappeared in the following two cycles. This observation certificated a series of electrolyte anion reductions involving lithium ions reacted to form SEI films. The initial discharge specific capacity reached relatively high 1516 mA h g^{-1} following with low initial coulomb efficiency of 48.9 % (Coulomb efficiency, Fig. S5). The electrode irreversible capacity of 774 mA h g^{-1} was probably associated with the formation of SEI films and a series of side reactions caused by the decomposition of electrolyte.[38] Except for the first discharge profile, the following discharge and charge curves have similar features and tendencies, indicating a reversible process of lithiation/delithiation from the SnO_x NAs@TiO_2 anode. However, even though the SnO_x NAs were completely encapsulated by the TiO_2 layers, the volume expansion of SnO_x could be restricted but still existed, some of SnO_x nanocrystals might expand beyond the TiO_2 layer, leading to continuous capacity loss in the following cycles. Besides, the capacity loss between 1.0 V and 2.0 V was mainly ascribed to the degradation of amorphous TiO_2,[9] whereas the capacity loss below 1.0 V was contributed to SnO_x since the Li-Sn alloying reaction took place below 1.0 V. The reversible capacities still maintain 422 mA h g^{-1} and 350 mA h g^{-1} after 100th and 300th cycle, respectively.

The cycling performance of as-prepared SnO_x NAs@TiO_2 anode were evaluated by galvanostatic charge/discharge cycling at 200 mA g^{-1} current density as shown in Fig. 5c. It was observed that the capacity swiftly dropped down from 700 mA h g^{-1} to 480 mA h g^{-1} after 50 cycles and began to keep much more stable after 50th cycle. The coulomb efficiency had increased to above 95% after the first cycle and maintains above 98% after the 10th cycles. The fade rate per cycle before the 50th cycle was 0.64 % and decreased to 0.11 % from the 50th to the 300th cycle. The reversible capacity eventually sustained at 350 mA h g^{-1} after 300 cycles. The theoretical designed capacity of SnO_x NAs@TiO_2 electrode (contains 63.6 wt % SnO_x and 36.4 wt % TiO_2 analyzed by ICP measurement) was calculated to 628 mA h g^{-1} ($780\times0.8\times0.636+875\times0.2\times0.636+330\times0.364=628$). The capacity retained nearly 55.7% of the designed capacity after 300 cycles, which is quite an improvement in the Sn-based materials anode. In contrast, we prepared pure SnO_x and TiO_2 NAs for comparison. The SnO_x NAs was prepared by FSP with the same conditions except the quenching ring went through $SnCl_4$ vapors instead of $TiCl_4$. The introducing of $SnCl_4$ ensured the particle size of SnO_x NAs were similar with SnO_x NAs@TiO_2. The TiO_2 NAs were synthesized by FSP with only ethanol combustion while quenching ring went through $TiCl_4$. The morphology and structure of SnO_x and TiO_2 were characterized in the TEM and SEM images in Figure S6. One on hand, the discharge capacity of SnO_x electrode is higher than SnO_x NAs@TiO_2 before 25th cycle because of pure SnO_x with higher energy density while the capacity sharply dropped to 200 mA h g^{-1} after 70th cycle. As mention above, especially for the condition that no protection of TiO_2 layer existed, the SnO_x NAs suffered from volume expansion of Li_xSn alloying reaction, resulting in deteriorated pulverization and huge capacity loss. On the other hand, the cycling performance of TiO_2 anode was stable, but the reversible

Cite this: DOI: 10.1039/c0xx00000x

www.rsc.org/xxxxxx

ARTICLE TYPE

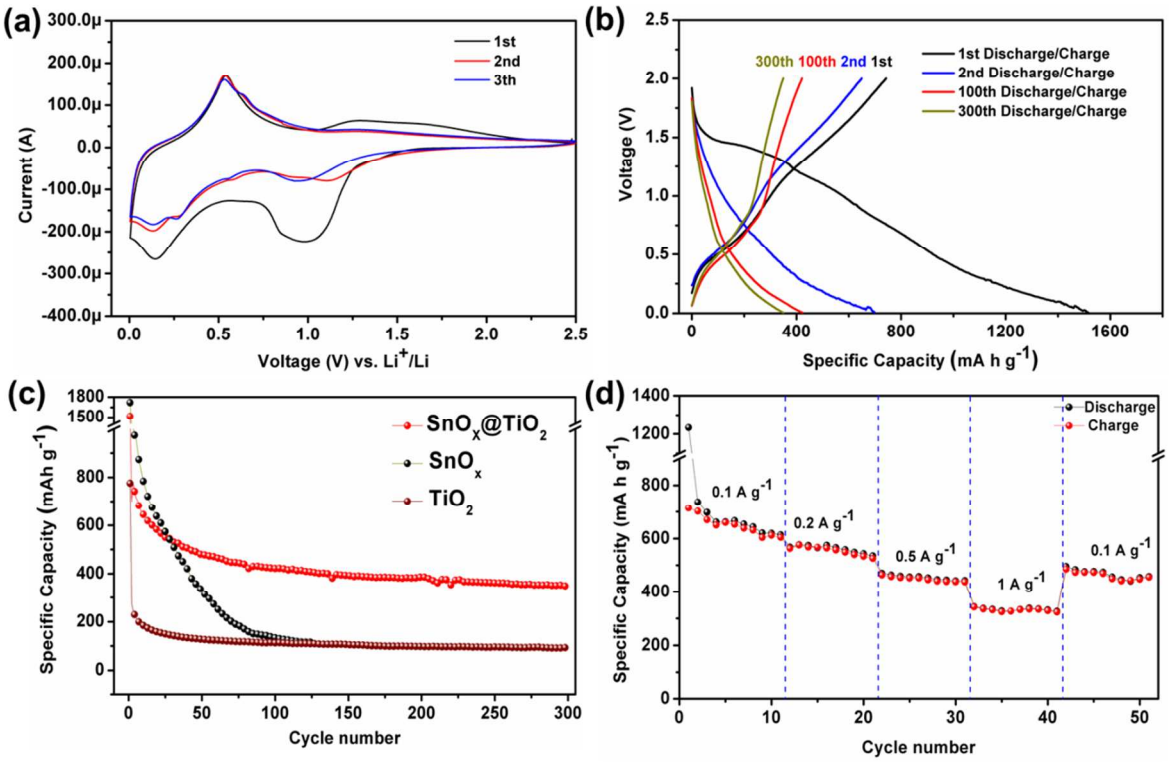

Fig. 5 (a) Cyclic voltammograms of SnO_x NAs@TiO_2 electrode in the voltage range of 2.5 V-0.01 V (versus Li/Li^+) at 0.2 mVs^{-1} scanning rate; (b) Galvanostatic charge/discharge curves of SnO_x NAs@TiO_2 anode; (c) Cycling performance of SnO_x NAs@TiO_2 and SnO_x and TiO_2 anodes at a current density of 200 mA g^{-1}; (d) Rate performance of SnO_x NAs@TiO_2 electrode at the current density of 100, 200, 500, 1000 and 100 mA g^{-1}, respectively.

capacity was below 100 mA h g^{-1} since the theory energy density of TiO_2 was relatively low (Coulomb efficiency of SnO_x and TiO_2 electrodes, Fig. S7). The morphology of SnO_x NAs@TiO_2 and SnO_x NAs anode after 50 cycles has been demonstrated by ex-situ TEM. As shown in the Fig. S8a and S8b, the structure of SnO_x NAs@TiO_2 after 50 cycles still remained the aggregates and the aggregations were independently dispersive. On the contrary, the volume expansion and deteriorated pulverization of SnO_x NAs could be obviously seen without protection of TiO_2 layer (Fig. 8c, 8d). Besides, the existence of TiO_2 layer could restrain the coacervation of SnO_x NAs though the size of each SnO_x nanocrystal grew larger after 50 cycles, leading to capacity loss in the first 50 cycles. Compared to the SnO_x or TiO_2 NAs electrode, the superior cycling performance and reversible capacity of SnO_x NAs@TiO_2 were ascribed to the design of active component and the core-shell structure of SnO_x-TiO_2. The amorphous TiO_2 layer not only protected the SnO_x from volume change in the cycling, but also possessed a rapid diffusion rate for insertion of Li^+.

Furthermore, the rate performance of SnO_x NAs@TiO_2 anode under the condition of same discharge and charge current densities were presented. The discharge capacity remained above 610 mA g h^{-1} in the current density of 100 mA g^{-1} before the 10th cycle. Although the capacity decreased to 543, 442, 332 and 458 mA g h^{-1} with the varying current density of 200, 500, 1000, 100 mA g^{-1}, and the decay tendency of capacity decreased slowly with increasing current density, indicating an excellent rate capacity performance, which is attributed to the ultrasmall size of SnO_x NAs. The nanocrystallines of SnO_x resulted in a high efficient Li^+ transportation pathway for insertion and diffusion of Li^+ during the cycling.

Electrochemical impedance spectroscopy (EIS) measurement was investigated to further identify the resistance of SnO_x NAs@TiO_2 electrode. Fig. 6 displayed the Nyquist plots (Z' vs. -Z", which refer to the real and imaginary parts of the cell impedance, respectively) of SnO_x NAs@TiO_2 before and after 50th discharge/charge rate performance cycle. Each Nyquist plot was composed of a depressed semi-circle in high frequency (10^5-200 Hz) and a linear line in the low frequency (below 200 Hz) referred to Warburg region (W). In the equivalent circuit (inset of Fig. 6), R_Ω and R_{ct} are the ohmic resistance which referred to integral resistance (including the electrolyte, separator, electrical contacts resistance) and charge transfer resistance, respectively.[39] The ohmic resistance before cycling (R_Ω = 547.2 Ω) was much higher than the ones after 50th cycles (R_Ω = 40.8 Ω, inset of Fig. 6), which was mainly caused by the lack of electrolyte wetting in the electrode materials before cycling. After the formation of SEI

film and the process of activation during the cycling, the ohmic resistance greatly decreased. The small value of 40.8 Ω explained the excellent rate performance of SnO_x NAs@TiO_2 electrode, implying it had a rapid Li^+ diffusion with assistant of nanoscale size of SnO_x NAs and the encapsulated amorphous TiO_2 layer.

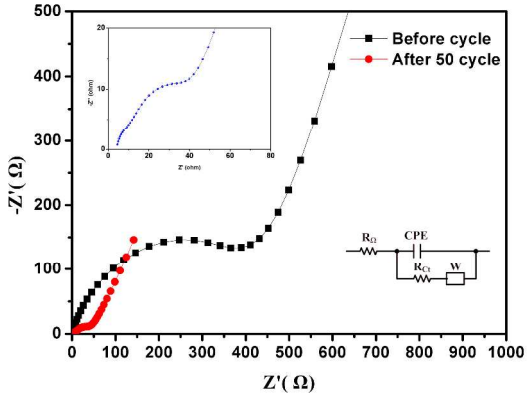

Fig. 6 Nyquist plots of SnO_x NAs@TiO_2 electrodes in thefrequency range from 0.01 Hz to 10^5 Hz before and after 50th cycles.

Conclusions

In summary, we have fabricated core-shell structure SnO_x NAs@TiO_2 by a one-step FSP route. The SnO_x NAs are constituted of SnO_x nanocrystals with 5-10 nm diameters and encapsulated by thin amorphous TiO_2 layer. The hydrolysis reaction temperature of $TiCl_4$ is controlled to prepare amorphous TiO_2, which was in situ coated on the SnO_x NAs. The SnO_x NAs@TiO_2 anode exhibits 350 mA h g^{-1} after 300 cycles at a current density of 200 mA g^{-1}, which is much superior to pure SnO_x NAs and TiO_2 NAs. Even at as high as 1A g^{-1}, the capacity still maintains above 332 mA h g^{-1}. The improved electrochemical performance is mainly ascribed to ultrasmall size of SnO_x NAs, core-shell structure with TiO_2 protection layer and amorphous state of TiO_2, realizing the confinement of Li-Sn alloy expansion and rapid Li diffusion rate.

Acknowledgment

This work was supported by the National Natural Science Foundation of China (21176068, 21236003), the Shanghai Rising-Star Program (13QA1401100), the Basic Research Program of Shanghai (11JC1403000, 14JC1490700), the Special Research Fund for the Doctoral Program of Higher Education of China (20120074120004) and the Fundamental Research Funds for the Central Universities.

Notes and references

[a] *Key Laboratory for Ultrafine Materials of Ministry of Education, School of Materials Science and Engineering, East China University of Science and Technology, Shanghai 200237, China. Fax: +86 21 6425 0624; Tel: +86 21 6425 0949; E-mail: czli@ecust.edu.cn ; huyanjie@ecust.edu.cn*
[b] *Shanghai Nanotechnology Promotion Center, Shanghai 200237, China*

† Electronic Supplementary Information (ESI) available: Schematic diagram of FSP equipment. TEM, particle size distribution, TGA, BET of as-prepared SnO_x NAs@TiO_2. Coulomb efficiency of SnO_x NAs@TiO_2 electrode. TEM and SEM images of SnO_x and TiO_2 NAs. See DOI: 10.1039/b000000x/

1. M. Armand and J. M. Tarascon, *Nature*, 2008, **451**, 652.
2. P. G. Bruce, B. Scrosati and J. M. Tarascon, *Angew. Chem. Int. Ed.*, 2008, **47**, 2930.
3. J. B. Goodenough and Y. Kim, *Chem. Mater.*, 2010, **22**, 587.
4. C. W. Sun, S. Rajasekhara, J. B. Goodenough and F. Zhou, *J. Am. Chem. Soc.*, 2011, **133**, 2132.
5. B. K. Guo, X. Q. Wang, P. F. Fulvio, M. F. Chi, S. M. Mahurin, X. G. Sun and S. Dai, *Adv. Mater.*, 2011, **23**, 4661.
6. X. Li and C. Wang, *J. Mater. Chem. A*, 2013, **1**, 165.
7. S. J. Han, B. C. Jang, T. Kim, S. M. Oh and T. Hyeon, *Adv. Funct. Mater.*, 2005, **15**, 1845.
8. L. Y. Liang, Z. M. Liu, H. T. Cao and X. Q. Pan, *ACS Appl. Mater. Interf.*, 2010, **2**, 1060.
9. Y. M. Lin, R. K. Nagarale, K. C. Klavetter, A. Heller and C. B. Mullins, *J. Mater. Chem.*, 2012, **22**, 11134.
10. H. G, R. Mao, D. X. Tian, W. Wang, D. P. Zhao, X. J. Yang and S. X. Wang, *J. Mater. Chem. A*, 2013, **1**, 3652.
11. G. Ji, B. Ding, Z. Sha, J. S. Wu, Y. Ma and J. Y. Lee, *Nanoscale*, 2013, **5**, 5965.
12. H. Liu, R. Z. Hu, W. Sun, M. Q. Zeng, J. W. Liu, L. C. Yang and M. Zhu, *J. Power Sources*, 2013, **242**, 114.
13. W. J. Zhang, *J. Power Sources,* 2011, **196**, 13.
14. L. P. Xu, C. J. Kim, A. K. Shukla, A. G. Dong, T. M. Mattox, D. J. Milliron and J. Cabana, *Nano Lett.*, 2013, **13**, 1800.
15. X. S. Zhou, Z. H. Dai, S. H. Liu, J. C. Bao and Y. G. Guo, *Adv. Mater.*, 2014, **26**, 3943.
16. X. S. Zhou, L. J. W and Y. G. Guo, *Adv. Mater.*, 2013, **25**, 2152.
17. D. H. Chen and R. A. Caruso, *Adv. Funct. Mater.*, 2013, **23**, 1356.
18. W. S. Wang, Q. Sa, J. H. Chen, Y. Wang, H. J. Jung and Y. D. Yin, *ACS Appl. Mater. Interfaces*, 2013, **5**, 6478.
19. S. B. Park, S. D. Seo, S. W. Lee, S. W. Seo, K. S. Park, C. W. Lee, D. W. Kim and K. S. Hong, *J. Phys. Chem. C*, 2012, **116**, 21717.
20. X. M. Wu, S. C. Zhang, L. L. Wang, Z. J. Du, H. Fang, Y. H. Ling and Z. H. Huang, *J. Mater. Chem.*, 2012, **22**, 11151.
21. C. Guan, X. H. Wang, Q. Zhang, Z. X. Fan, H. Zhang and H. J. Fan, *Nano Lett.*, 2014, **14**, 4852.
22. J. H. Jeun, K. Y. Park, D. H. Kim, W. S. Kim, H. C. Kim, B. S. Lee, H. G. Kim, W. R. Yu, K. Kang and S. H. Hong, *Nanoscale*, 2013, **5**, 8480.
23. G. Ji, B. Ding, Y. Ma and J. Y. Lee, *Energy Technol.*, 2013, **1**, 567.
24. M. V. Koudriachova, N. M. Harrison and S. W. de Leeuw, *Phys. Rev. Lett.*, 2001, **86**, 1275.
25. M. Wagemaker, A. P. M. Kentgens and F. M. Mulder, *Nature*, 2002, **418**, 397.
26. M. Wagemaker, R. van de Krol, A. P. M. Kentgens, A. A. van Well and F. M. Mulder, *J. Am. Chem. Soc.*, 2001, **123**, 11454.
27. H. T. Fang, M. Liu, D. W. Wang, T. Sun, D. S. Guan, F. Li, J. G. Zhou, T. K. Sham and H. M. Cheng, *Nanotechnology*, 2009, **20**, 225701.
28. Y. F. Li, Y. J. Hu, H. Jiang and C. Z. Li, *Nanoscale*, 2013, **5**, 5360.
29. X. Y. Hou, Y. J. Hu, H. Jiang, J. C. Huo, Y. F. Li and C. Z. Li, *J. Mater. Chem. A*, 2013, **1**, 13814.
30. R. Strobel and S. E. Pratsinis, *J. Mater. Chem.*, 2007, **17**, 4743.
31. W. Y. Teoh, R. Amal and L. Mädler, *Nanoscale*, 2010, **2**, 1324.
32. Y. F. Li, Y. J. Hu, H. Jiang, X. Y. Hou and C. Z. Li, *RSC Adv.*, 2013, **3**, 22373.
33. F. Gu, W. J. Huang, S. F. Wang, X. Cheng, Y. J. Hu and C. Z. Li, *J. Power Sources*, 2014, **268**, 922.
34. J. C. Huo, Y. J. Hu, H. Jiang, W. J. Huang and C. Z. Li, *J. Mater. Chem. A*, 2014, **2**, 8266.
35. D. Deng and J. Y. Lee, *Angew. Chem., Int. Ed.* 2009, **48**, 1660.
36. M. Marcinek, L. J. Hardwick, T. J. Richardson, X. Song and R. Kostecki, *J. Power Sources*, 2007, **173**, 965.
37. Y. S. Jung, K. T. Lee, J. H. Ryu, D. Im and S. M. Oh, *J. Electrochem. Soc.*, 2005, **152**, A1452.
38. Y. M. Lin, P. R. Abel, D. W. Flaherty, J. Wu, K. J. Stevenson, A. Heller and C. B. Mullins, *J. Phys. Chem. C*, 2011, **115**, 2585.
39. X. Y. Hou, H. Jiang, Y. J. Hu, Y. F. Li, J. C. Huo and C. Z. Li, *ACS Appl. Mater. Interfaces*, 2013, **5**, 6672.